Microstructure of epitaxial $La_{0.7}Ca_{0.3}MnO_3$ thin films grown on $LaAlO_3$ and $SrTiO_3$

C. J. Lu[a] and Z. L. Wang[b]
Beijing Laboratory of Electron Microscopy, Center for Condensed Matter Physics and Institute of Physics, Chinese Academy of Sciences, P.O. Box 2724, Beijing 100080, People's Republic of China

C. Kwon
Department of Physics and Astronomy, California State University-Long Beach, Long Beach, California 90840

Q. X. Jia
Mail Stop K763, Los Alamos National Laboratory, Los Alamos, New Mexico 87545

(Received 11 January 2000; accepted for publication 7 July 2000)

Epitaxial $La_{0.7}Ca_{0.3}MnO_3$ (LCMO) thin films of a thickness ~170 nm were grown on (001) $LaAlO_3$ (LAO) and (001) $SrTiO_3$ (STO) substrates by pulsed laser deposition. Transmission electron microscopy and associated techniques have been applied to investigate the microstructures introduced by lattice mismatch that are responsible for the observed differences in properties between these two films. Numerous secondary phase rods were observed in both films. For the LCMO/LAO film, Ca-deficient secondary-phase rods originated in the film after a thickness of about 25 nm and were found to be responsible for relieving in-plane compressive stress during the island growth. In the case of STO substrate, however, almost all of secondary-phase rods initiated at the film–substrate interface. The lattice mismatch between LCMO and STO is relaxed into regions of good coherent fit separated by such secondary phases, possibly resulting from interfacial reaction. The two types of substrates lead to the formation of two different crystallographic domain structures in the LCMO films. The film on LAO exhibits an almost pure [110] out-of-plane texture with 90° domains in plane. In contrast, the film grown on STO consists of mixed domains of [001] and [110] orientations and is dominated by [001] texture. © *2000 American Institute of Physics.* [S0021-8979(00)03620-3]

I. INTRODUCTION

Ever since the discovery of colossal magnetoresistance (CMR) in perovskite type $Ln_{1-x}A_xMnO_3$ (Ln=lanthanides, A=alkaline earth elements or Pb), there has been enormous interest in these materials both in bulk and thin films forms.[1–5] Recently, the observation of large magnetoresistance (MR) effects in epitaxial manganite thin films has renewed interest in the doped manganite perovskite materials for potential magnetic random access memory and read-head applications.[6–9] However, before any significant practical applications are realized, critical properties of the CMR materials must be improved. For example, the MR values are high at insulator–metal transition temperature and in high magnetic field (several Tesla), but the response close to room temperature and in low field is very weak (<1%).

In doped Mn oxides, magnetism and electronic conduction are closely related. The CMR properties could be related to the double exchange mechanism,[10] which depends on the Mn–O–Mn bond distance and angle. Recent theoretical and experimental work has shown that the double exchange model is not sufficient to explain the magnitude of the magnetoresistance.[11–13] Well-characterized experimental data are crucial for developing and verifying theoretical models and *vice versa*. These models could show a way towards optimized perovskite materials for future applications. This study aims to clarify the role of lattice mismatch between the film and substrate in the growth and properties of CMR thin films.

The importance of lattice distortions on magnetic properties has been established both theoretically and experimentally. Several groups have shown that properties such as the Curie temperature T_c, resistivity, and the MR effect are extremely sensitive to the chemical pressure from the alkaline-earth substitution of the rare-earth ions, as well as to hydrostatic pressure.[14–17] Therefore, it is not surprising that lattice mismatch between the film with the substrate imposes a strain that greatly affects the magnetic properties of doped manganite thin films. Recently, several groups have reported that lattice strain affects the peak resistance temperature T_p, resistivity, magnetic, and MR properties of $Pr_{0.67}Sr_{0.33}MnO_3$,[18] $La_{0.7}Sr_{0.3}MnO_3$,[19] $La_{0.7}Ca_{0.3}MnO_3$,[7,8,20] and $La_{0.8}Ca_{0.2}MnO_3$ thin films.[21,22] Wang *et al.*[18] obtained large low-field MR in strained $Pr_{0.67}Sr_{0.33}MnO_3$ ultrathin films and found very different effects of compressive and tensile strain on the magnetic and the low-field MR properties.

[a]Also at Department of Physics, Hubei University, Wuhan 430062, People's Republic of China: electronic mail: cjlu@mpi-halle.de
[b]Also at School of Materials Science and Engineering, Georgia Institute of Technology, Atlanta, GA 30332-0245.

Magnetic anisotropies in thin films have been interpreted in terms of substrate-induced stress.[19–22] The anomalous anisotropic low-field MR properties can be qualitatively explained based on the strain-induced magnetic anisotropy.[18] This interpretation seems to be reasonable and likely to be correct, but the mechanism based on strain alone may not be sufficient to account for all aspects of the experimental results such as the thickness and temperature dependencies of the magnetic and low-field MR properties.[18,21] In fact, crystallographic domain orientation can also play an important role in determining magnetic anisotropy.[21,22] Theoretical analysis predicted that the T_c of CMR thin films is extremely sensitive to biaxial strain: a 1% biaxial strain would cause a 10% shift in T_c.[23] In contrast, experimental results did not show such a high sensitivity.[8,19–21] Thus, other factors such as structural defects and domain structure must also be considered in order to analyze quantitatively the properties of CMR thin films on different substrates. It has been reported that the $SrRuO_3$ films grown by pulsed laser deposition (PLD) or $LaAlO_3$ and $SrTiO_3$ exhibit quite different domain structures and structural defects.[24] We have examined the microstructure in epitaxial $La_{1-x}Sr_xCoO_{3-\delta}$ CMR thin films in detail.[25–27] To the best of our knowledge, however, very few detailed studies have been performed on microstructural features such as defects and orientation disorder in doped manganite thin films.[20,28–30]

We have reported previously that the transport and magnetic properties of epitaxial $La_{0.7}Sr_{0.3}MnO_3$ films depend on the lattice mismatch between the substrate and the film.[19] In the present work, we report studies of the strain states, nonstoichiometric phases, crystallographic domain structure, interfacial structure and reaction, and transport properties of the LCMO thin films as a function of lattice mismatch with substrate. The main focus of this study concerned transmission electron microscopy (TEM) investigation of growth-induced secondary phases and of the oriented domains formed in the LCMO films. The $La_{0.7}Ca_{0.3}MnO_3$ composition ($T_c \sim 265$ K for bulk) was chosen since it has potential interest for room temperature applications. Two LCMO thin films were prepared on LAO and STO, respectively. These two substrates were used to provide two different types of lattice mismatch for the growth of LCMO films, -1.7% with LAO and $+1.2\%$ with STO. While a LAO substrate imposes an in-plane compressive stress on the film, a STO substrate imposes a corresponding biaxial tensile stress.

Since STO is not completely inert to LCMO, the interfacial reaction is an important factor influencing the growth and quality of the LCMO films. In this article, the interfacial structure and interfacial reaction of the PLD-grown LCMO/STO film are also investigated in detail.

II. EXPERIMENT

The LCMO thin films on (001) LAO and (001) STO substrates were grown by pulsed laser deposition using a XeCl excimer laser. For ease of comparison, the two samples were deposited at the same time in order to eliminate other extrinsic factors. The laser energy density at the target was ~ 2 J/cm^2. The heater block temperature was 800 °C during deposition. The oxygen pressure during deposition was 400 mTorr and was increased to 1 atm on for cooldown after deposition. The thickness of the thin films was about 170 nm. No further thermal treatment was performed on the samples after the deposition. The resistance was measured by the four-probe transport method.

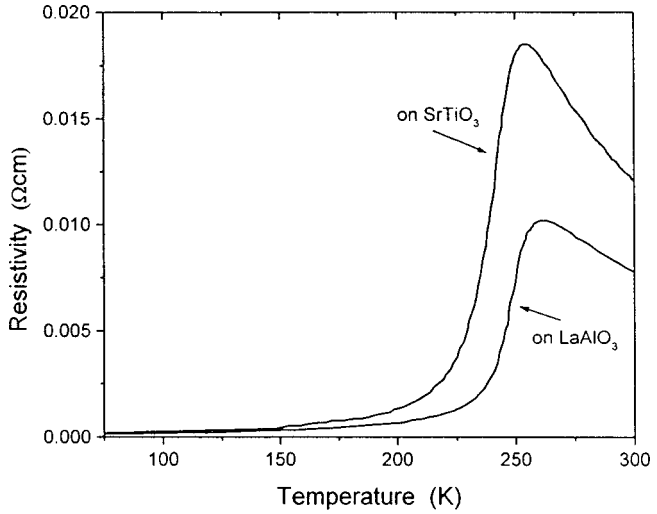

FIG. 1. Resistivity vs temperature for the LCMO thin films grown on LAO and STO substrates.

The x-ray diffraction (XRD) patterns of the films were recorded on a Rigaku D/max-2400 x-ray diffractometer using Cu $K\alpha$ radiation. The scanning step size was 0.02° and count times were 2 s. The out-of-plane lattice parameters of the films were calculated using the nonlinear least square fitting method. The substrate (002) peak position was used as the calibration standard. Surface morphology and grain size analyses were performed on a Digital Instrument Nanoscope III atomic force microscope.

The thin films were examined by TEM in both cross sectional and plan view. The cross-sectional slices for TEM investigation were obtained by cutting the LCMO/STO and LCMO/LAO samples along the [100] direction of LAO and STO, and then gluing the cut slides face-to-face by joining the LCMO surfaces. TEM specimens were prepared by mechanical grinding, polishing and dimpling, followed by Ar-ion milling at 4.5 kV. Selected area electron diffraction (SAED) patterns, high resolution electron microscopy (HREM) images and electron energy loss spectroscopy (EELS) spectra were recorded in a Philips CM200 FEG electron microscope operated at 200 kV.

III. RESULTS

A. Matrix properties of the two films

The resistivity versus temperature for the LCMO films grown on LAO and STO are shown in Fig. 1. The film on STO showed higher room temperature resistivity ($\rho \sim 0.012\,\Omega$ cm), pronounced semiconductor-like behavior in the range of 300–255 K, and a semiconductor–metal transition at $T_p \approx 255$ K. For the film on LAO, the resistivity decreased by a factor of around two compared with the film on STO, and the T_p shifts to 261 K. The T_p values of our films

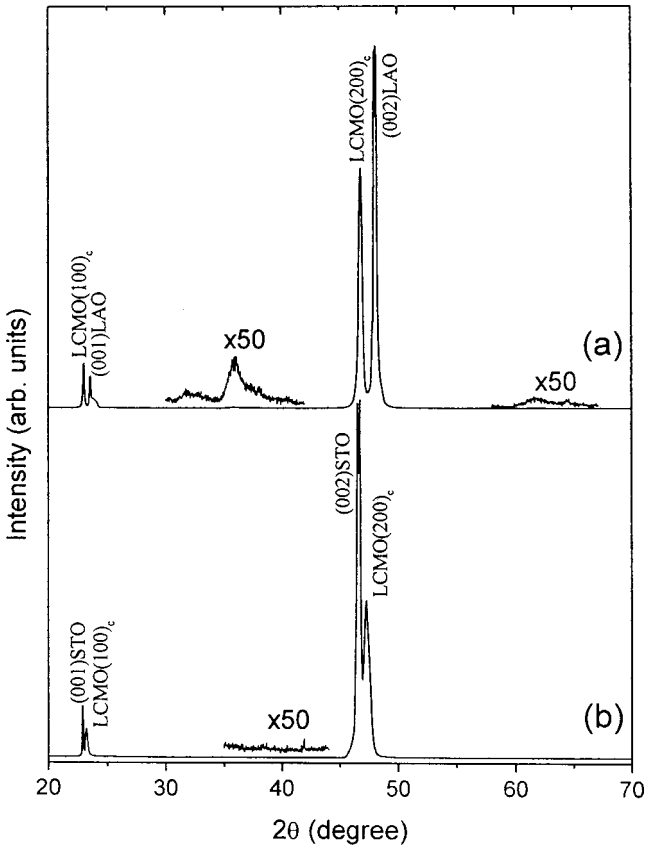

FIG. 2. XRD patterns of the LCMO films grown on (a) (001) LAO, and (b) (001) STO substrates. The peaks of the films are indexed based on the pseudo-cubic perovskite unit cell, denoted by subscript ''*c*.''

are lower than the T_p value of 290 K reported on LCMO($x=0.3$) films deposited on LAO by magnetron sputtering.[8] The transition temperature for the film on LAO is higher than that for the film on STO. This observation is consistent with previous reports,[21,31,32] but the difference between the two T_p values for our films (only ~6 K) is much smaller than those reported values (~35 K). These differences may be due to the different experimental details and microstructures between the films in this study and in previous studies.

The XRD patterns of the films grown on LAO and STO are shown in Figs. 2(a) and 2(b), respectively. For the LCMO/STO film, the only peaks observed in the θ-2θ scan are from the substrate, and the film (110) and/or (002) reflections. Even if the intensity is increased by a factor of 50, no other peaks can be seen except a very weak and narrow peak at $2\theta=41.9°$. Because the splitting between the (110) and (002) reflections of the orthorhombic LCMO is too small to be resolvable, the peaks of the films are indexed based on the single perovskite unit cell. In this article, the subscript ''*c*'' denotes the pseudocubic perovskite unit cell. For the film on LAO, it can be seen from Fig. 2(a) that several very weak reflections appear at $2\theta=31.96°$, 36.14°, and 61.82°, in addition to the strong reflections from the substrate, and the LCMO film (110) and/or (002). These weak and broad peaks cannot be indexed with the orthorhombic LCMO (see JCPD No. 44-1040 and No. 35-1353), indicating the existence of a small amount of secondary phases in the film.

TABLE I. Lattice parameters of $La_{0.7}Ca_{0.3}MnO_3$ thin films on different substrate materials in comparison to bulk sample values.

Substrate	Misfit	Out-of-plane lattice parameter (observed)	In-plane lattice parameter (calculated)	FWHM of $(100)_c$ peak (°)
$LaAlO_3$ (3.792 Å)	−1.7%	3.893 Å	3.841 Å	0.188
$SrTiO_3$ (3.905 Å)	1.2%	3.851 Å	3.862 Å	0.235
Bulk $La_{0.7}Ca_{0.3}MnO_3$[a]		3.858 Å		

[a]See Ref. 33.

The lattice parameters (based on the single perovskite cell) of the two films and the corresponding bulk are listed in Table I. The out-of-plane lattice parameter of the film on LAO, calculated from the least-square fitting of the observed $(002)_c$ reflections, is larger than the bulk cell parameter, while that of the film on STO is smaller than the bulk cell parameter. This indicates an influence of strain resulting from lattice mismatch with the substrate. Assuming that the film is strained from the ideal bulk structure, which has a volume of $(3.858\ Å)^3$,[3,33] the in-plane lattice parameters of the films (see Table I) can be calculated. For these films with the thickness of ~170 nm, such an assumption is reasonable according to Rao *et al.*'s report.[21] Note that in general the perovskite unit cell volume in LCMO films is not conserved, i.e., the unit cell volume of the films and its distortions may not be the same as those of the bulk.[21]

It can also be seen from Fig. 2 that the $(100)_c$ reflection of the film on STO is remarkably broader than that for the film on LAO. The measured full width at half maximum (FWHM) of the $(100)_c$ peak in the XRD patterns for the films on LAO and STO are ~0.188° and 0.235°, respectively, as shown in Table I. This suggests an increased mosaic spread in the film grown on STO owing to the formation of mixed domains of [110] and [001] orientations, as confirmed by our TEM observations (see Sec. III C).

The surface morphology and growth mechanism were also studied using atomic force microscopy (AFM). Figures 3(a) and 3(b) show the typical AFM images of the LCMO films grown on LAO and STO, respectively. For both films, an island growth surface morphology was observed. The average grain sizes in the films on LAO and STO are ~80 and 100 nm, respectively. The peak to valley surface roughness of ~29.2 nm was observed over a 4 μm^2 area for the film on LAO, while ~23.9 nm for the film on STO. The root mean square (rms) roughness of the films on LAO and STO are ~3.8 and 3.2 nm, respectively. The surface roughening is due to strain relaxation and island growth rather than the particulates generated during the growth procedure, since very few loose particles or boulders were found at or near the surface. These results are in agreement with our cross-sectional TEM observation, as discussed in Sec. III B.

B. Secondary phase, interface and defect structures

1. LCMO film on LAO

Figure 4(a) shows a low-magnification cross-sectional TEM image of the LCMO film grown on LAO. The SAED patterns recorded from the cross-sectional TEM specimen, as

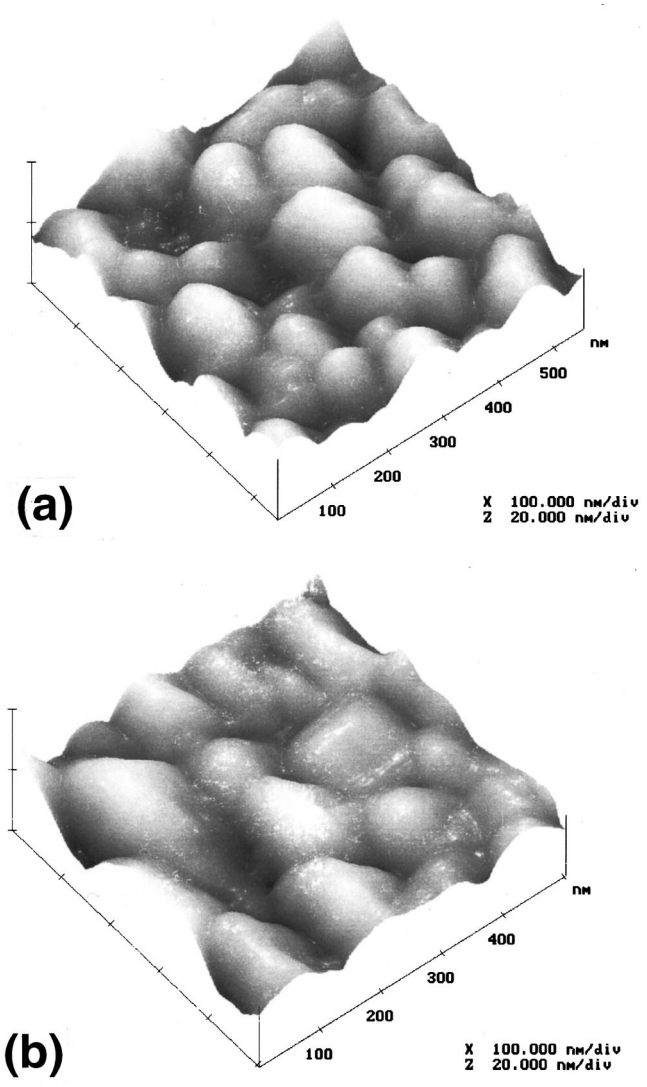

FIG. 3. AFM images of the LCMO films grown on (a) LAO, and (b) STO.

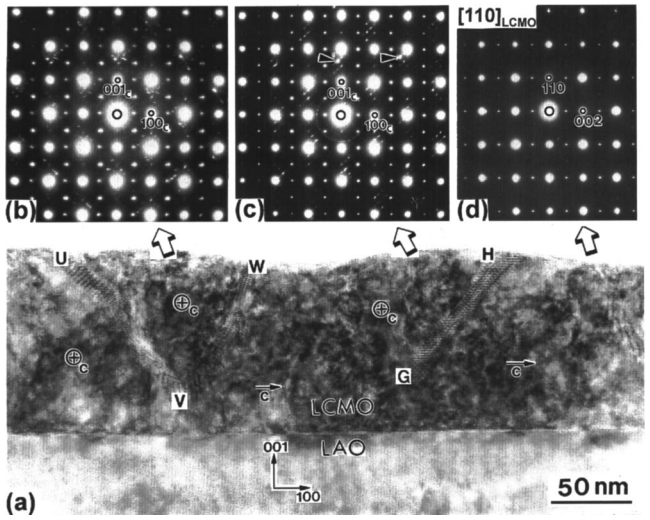

FIG. 4. (a) Low-magnification TEM image showing the cross-sectional structure of the LCMO/LAO film. The growth-induced nonstoichiometric secondary phase can be seen at UVW and GH in LCMO layer. Arrows indicate the *c* direction of individual orientation domains and a ring with a cross in it shows the end of an arrow normal to the image; (b), (c), and (d) are corresponding SAED patterns taken from three different areas in (a). Pattern (b) was taken from an area including the v-shaped UVW, (c) from an area surrounding the rod-shaped GH, and (d) from an area to the right of the GH. Patterns (b) and (c) are indexed based on the single perovskite cell. Note the double diffraction spots around the $(10\bar{1})_c$ and $(101)_c$ reflections.

shown in Figs. 4(b)–4(d), indicate that the LCMO layer is grown epitaxially on LAO and is multidomain oriented. Regarding the crystallographic domain structure formed in the film, this will be discussed in Sec. III C in more detail. It may be noted that numerous thin-wire shaped secondary phases are formed in the film after a thickness of about 25 nm and their diameters are about 10 nm, as shown in Fig. 4(a). Some of them are v-shaped such as that marked by UVW in Fig. 4(a) whereas others are rod shaped such as that marked by GH. The presence of moiré fringes at the secondary phase rods indicates that they are buried in the matrix of the film. The average spacings between these secondary phase rods is about 100 nm and thus the density of these rods is relatively high, although very few originate at the interface with the substrate.

EELS microanalysis indicates that the secondary phase rods are nonstoichiometric. Figures 5(a) and 5(b) show EELS spectra acquired from the film matrix and the secondary phases, respectively, where the Ca-$L_{2,3}$, O–K, Mn-$L_{2,3}$, and La-$M_{4,5}$ edges are in the displayed energy loss region. It can be seen that the Ca-$L_{2,3}$ edge of Fig. 5(b) is much less intense than in Fig. 5(a). Quantitative analysis indicates that the element ratio La:Ca:Mn:O at the secondary phase rods is about 0.8:0.2: 1.0:3.07, assuming that the film matrix is stoichiometric. Note that the measured element ratio is not the real chemical composition of the secondary phase, since it does not penetrate through the entire thickness of the cross-sectional TEM sample. However, it is sufficient to indicate the general trend of the deviation of the chemical composition of the secondary phase from the stoichiometric composition. Extensive EELS microanalysis indicates that almost

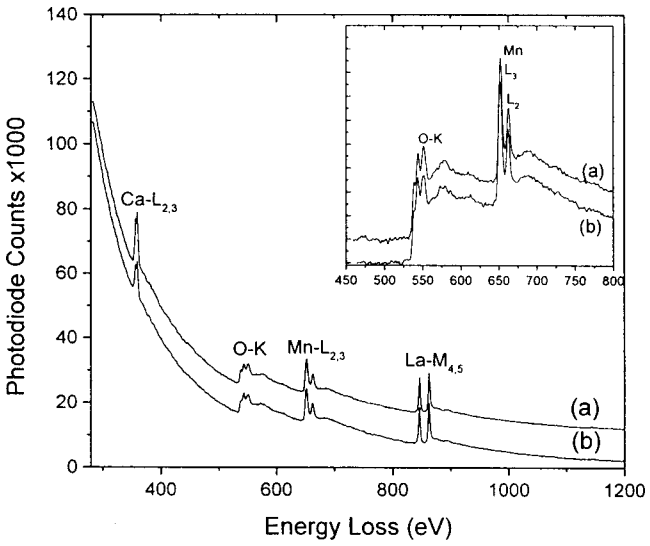

FIG. 5. EELS spectra obtained from (a) the matrix of the film and (b) the secondary phase GH in Fig. 4(a). The inset shows the corresponding EELS spectra of O–K and Mn–$L_{2,3}$ edges. The ratio of the integrated intensities at the near-edge regions $I_{Ca}:I_O:I_{Mn}:I_{La}$ is ~2.0:2.2:1.3:1.0 for spectrum (a) while it is about 1.2:2.0:1.1:1.0 for spectrum (b).

all the secondary phase rods in the film have a similar deviation of chemical composition from stoichiometric. Fine structures at the near-edge region reflect the density of states in the valence band. The three fine peaks observed in the O–K edge of LCMO indicate three valence states located below the edge of the conduction band. No remarkable differences can be seen from the fine structures of O–K or Mn-$L_{2,3}$ edges between the secondary phase rods and the film matrix, as shown in the inset of Fig. 5.

The rod-shaped grains are oriented near the $[101]_c$ direction (nearly 45° to the substrate surface), as shown in Fig. 4(a). Figure 4(d) shows the SAED pattern taken from the right-hand side of the rod GH and it is the [110] pattern for orthorhombic LCMO. The SAED pattern taken from an area including the secondary phase GH is shown in Fig. 4(c). This is a multidomain pattern and the $(100)_c$ and $(001)_c$ labels just indicate reflections of the type $\{100\}_c$. The precise indexing should depend on domain orientations (see Sec. III C). In fact, the superlattice reflection $1/2(100)_c$ in Fig. 4(c) can be indexed as the (001) reflection of the [110] pattern for orthorhombic LCMO [see Fig. 4(d)] and the $1/2(101)_c$ as the (100) reflection of the [001] pattern. Besides the primary reflections of LCMO matrix, many weak and regularly arranged spots are visible in Fig. 4(c) and they originate from the rod-shaped secondary phase, and from the double diffraction between it and the matrix. When dark field images were taken with the spots indicated by arrowheads, these rods showed bright contrast. The moiré fringe pattern of the rod GH consists of two sets of parallel fringes, as shown in Fig. 4(a). One is nearly along the $[101]_c$ direction and the another along $[100]_c$. The moiré fringe spacings are in excellent agreement with the double-diffraction pattern in Fig. 4(c). Two of the reciprocal space basis vectors of the rod are 3.29 nm^{-1} and the angle between the two is 90°. This means that the rod has at least two sets of planes. Their interplanar distances are ~0.304 nm and the included angle between them is 90°. The presence of crossed translational moiré patterns at GH suggests that the rod is perfectly aligned with the film matrix, as confirmed by our HREM observation. Figure 6(a) shows the HREM image of the GH rod. The Fourier transform of the image, shown as an inset of Fig. 6(a), exhibits the presence of double-diffraction spots around the primary reflections $(101)_c$ and $(10\bar{1})_c$. They also surround the direct beam, although they are hidden in the flare from that beam in Fig. 4(c).

The two SAED patterns shown in Figs. 4(b) and 4(c) are similar. The difference between them is that diffraction spots coming from the secondary phases and double diffraction in Fig. 4(b) are elongated along different directions. It can also be seen from Fig. 4(a) that complex (including translational and rotational) moiré fringes are present at the secondary phase UVW. These demonstrate that the v-shaped secondary phase is not perfectly aligned with the film matrix and its lattice orientations are different from one part to another.

More importantly, however, almost all of the secondary phase rods do not originate at the film–substrate interface, but at a depth of 25–35 nm in the film and penetrate to the film surface. The thin layer below a thickness of ~25 nm is almost free of such rods. Figure 6(b) shows an enlarged

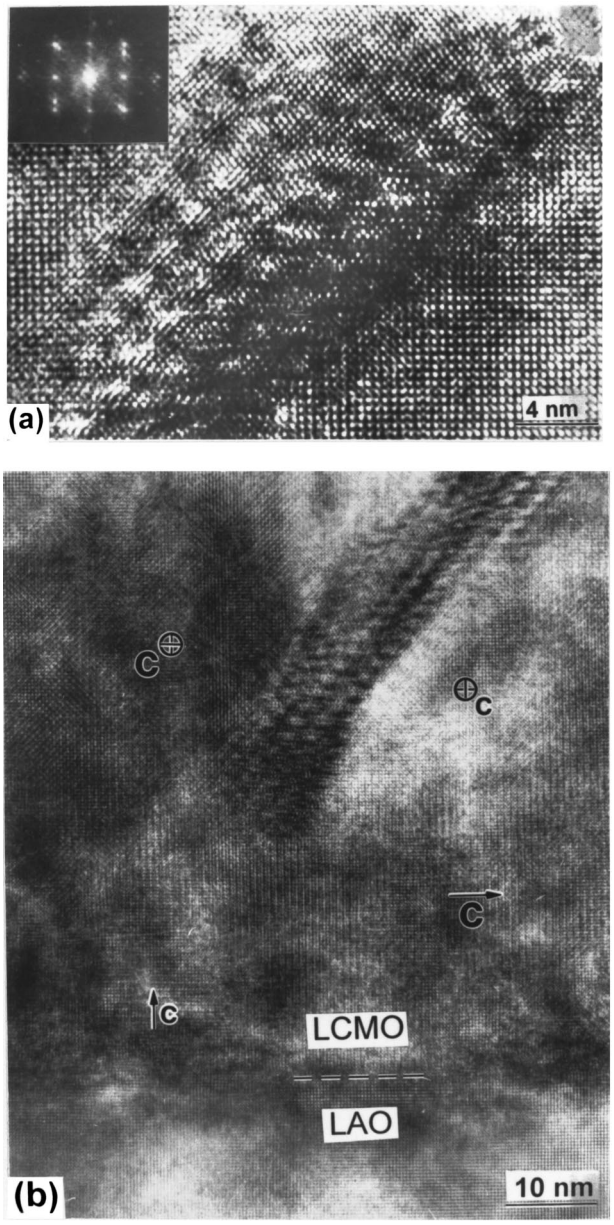

FIG. 6. (a) HREM image at the secondary phase GH in Fig. 4(a), along with the corresponding Fourier spectrum shown as an inset; (b) an enlarged image of GH at its early stage of formation. Arrows indicate the *c*-axis directions of orthorhombic LCMO. Note the presence of a small [001] oriented domain below GH.

TEM image at the beginning stage of the growth of the GH rod in Fig. 4(a) and no apparent interface reaction can be seen. A perfectly epitaxial layer with a thickness of about 25 nm is formed from the substrate–film interface. This suggests that the ideal epitaxy is preserved only within about the first 25 nm. The LCMO film on LAO grew layer-by-layer in the initial stage up to about 25 nm and changed to island growth, indicating a Stranski–Krastanov growth mode.

Clearly, those weak peaks in the XRD pattern of Fig. 2(a) come from the secondary phase rods shown in Fig. 4(a). Our EELS microanalysis suggests that the secondary phases seem to be $LaMnO_{3+\delta}$, $La_{0.9}Mn_{0.1}O_{3+\delta}$, or similar phases. These compounds do not have the two sets of planes with the interplanar distance of ~0.304 nm and the included angle of

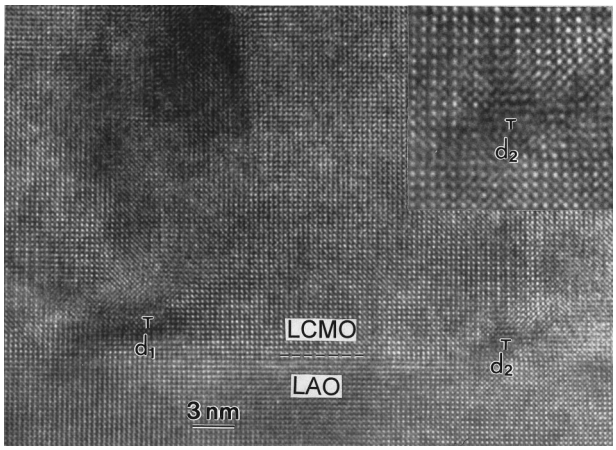

FIG. 7. Cross-sectional HREM image of LCMO/LAO interface showing the nonreactive and coherent growth of LCMO. Dislocations (T) are seen at the interface at an interval of ~27.7 nm. The inset is an enlarged image of a dislocation.

90°,[34] however, which was found by analysis of SAED patterns. Although the identity of the nonstoichiometric phase remains to be determined, the formation of such secondary phase rods can be attributed to relieve compressive stress in the plane of the film during the Stranski–Krastanov growth (see discussion in Sec. IV A).

Dislocations are usually produced at the interface to partially relieve the strain due to lattice mismatch between the film and substrate. Figure 7 shows a cross-sectional HREM image of the LCMO/LAO interface. The interface is atomically sharp without secondary phase or chemical reaction. Strain fields associated with interface dislocations are observed. The edge-type dislocations are created at the LAO side in order to match the constrained lattice and they are separated by ~27–29 nm. The distance between the two adjacent interface dislocations is expected to be

$$D = d_1 d_2 / (d_1 - d_2), \tag{1}$$

where d_1 and d_2 are the interplanar distances of the film and the substrate, respectively. If we assume the two lattices to be completely relaxed, the mismatch is about − 1.7%, requiring one interfacial dislocations every 22.1 nm spacing. In reality the mean separation of the interfacial dislocations is found to be ~27–29 nm. This means that a small part of the mismatch is adopted by elastic strain.

2. LCMO film on STO

Numerous secondary phase rods are also formed in the LCMO/STO film. Unlike the LCMO/LAO film, almost all rods observed were initiated at the film–substrate interface in the case of STO substrate. Some of them penetrated the entire thickness of the film, and the others ended in the bulk of the film. Figure 8(a) shows a low-magnification cross-sectional bright-field TEM image of the LCMO/STO film. Figure 8(b) is a SAED pattern taken from the LCMO film and STO substrate, whereas Fig. 8(c) is that of STO substrate. The lattice mismatch between the LCMO and STO is so small that the splitting between the reflections of STO and LCMO is hardly seen in the SAED pattern of Fig. 8(b). The

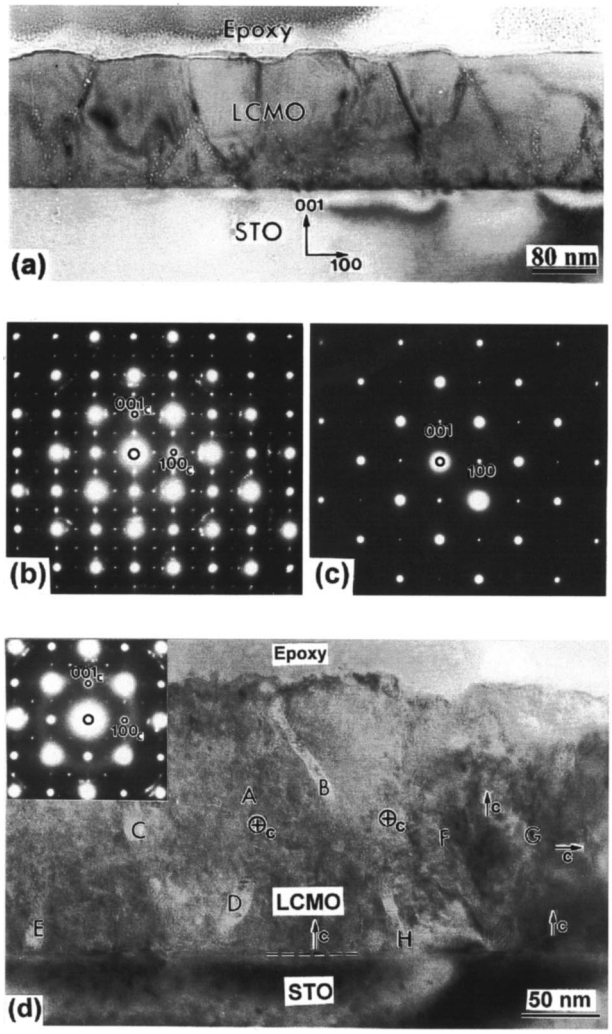

FIG. 8. (a) Low-magnification TEM off-axis image showing the cross-sectional structure of the LCMO film grown on STO, along with the SAED patterns taken from: (b) both the LCMO layer and STO, and (c) the STO substrate; (d) cross-sectional TEM on-axis image of the LCMO/STO film, along with the corresponding SAED pattern shown as the inset. Arrows indicate the *c* directions of individual orientation domains. Note that the two regions shown in (a) and (d) are very close but the former is much thinner than the latter. The SAED patterns are indexed based on the single perovskite cell. It can be seen from (a) and (d) that secondary phase rods are initiated at the film–substrate interface.

presence of superreflections $1/2(001)_c$, $1/2(100)_c$, and $1/2(101)_c$ is due to the mixed domain orientations of the orthorhombic LCMO. In addition to the primary reflections and super reflections, a few relatively intense spots and many weak spots are visible in Fig. 8(b) and they belong to the secondary phases. When dark field images were taken using these spots, not all parts of the secondary phase rods became bright at the same time, i.e., some parts of the rods were bright when a dark-field image was taken using one spot whereas they became dark when using another spot. This indicates that the rods do not have the same crystal structure and the same crystal orientation.

The thickness of the film is ~170 nm and the film surface is rough, as shown in Fig. 8(a). The average grain size and the peak-to-valley surface roughness are about 100 and 20 nm, respectively. These results are consistent with our

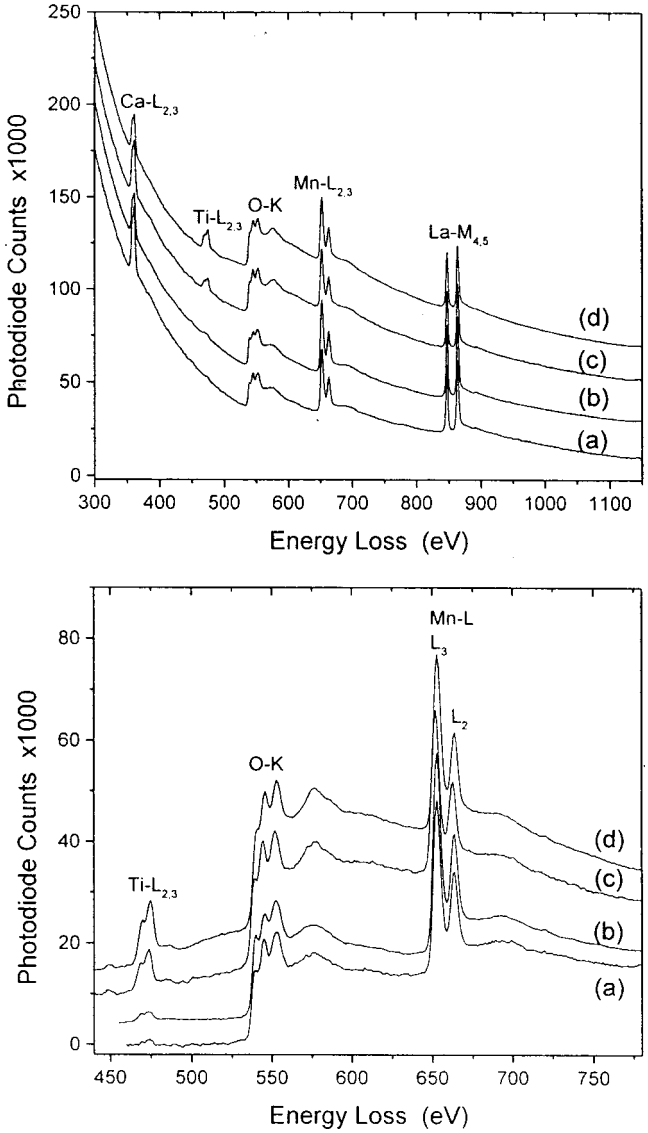

FIG. 9. EELS spectra acquired from four different positions in Fig. 8(d): (a) matrix of the film at the position marked by ''A,'' (b) rod B, (c) rod C, and (d) rod D. The lower figure shows the corresponding EELS spectra of Ti-$L_{2,3}$, O–K and Mn-$L_{2,3}$ edges.

previous AFM observations. It is of interest to note in Fig. 8(a) that the secondary phase rods are usually at the positions of grain boundaries if they can grow to the film surface.

Figure 8(d) shows a cross-sectional TEM image of the LCMO/STO film. The inset is the corresponding SAED pattern recorded from the LCMO layer, in which the amorphous ring is partly due to the glue above the film layer. The thickness of the secondary phase rods ranges from 8 to 12 nm, close to the diameter of the wire-shaped secondary phase formed in the LCMO/LAO film. The contrast of these rods is discontinuous. Moiré fringes can be seen occasionally at the rods, indicating that the width of the rods is not uniform. Sometimes it can be larger than the thickness of the TEM specimen (~25 nm).

In the case of the LCMO/STO film, interfacial reaction and elemental diffusion occur. Figures 9(a)–9(d) show the EELS spectra acquired from the positions marked by A, B, C, and D in Fig. 8(d), respectively. The lower figure of Fig. 9 shows the corresponding fine structures of Ti-$L_{2,3}$, O–K and Mn-$L_{2,3}$ edges. The three fine peaks observed in the O–K edges of indicate three discrete states located below the edge of the conduction band. No remarkable differences can be seen from the fine structures of O–K or Mn-$L_{2,3}$ edges between the secondary phases and the film matrix. However, a remarkable change of the Ti-$L_{2,3}$ edges can be seen in the EELS spectra (c) and (d) in Fig. 9. Ti-$L_{2,3}$ edges have also been detected in the EELS spectra acquired from rod B and even the matrix of the film, but they are very weak [see curves (b) and (a) in the lower figure of Fig. 9]. Another fact is that the O–K edges in spectra (c) and (d) of Fig. 9 are more intense than those in spectra (a) and (b). The EELS spectra in Fig. 9 were analyzed. The analysis result shows that the element ratios La: Ca:Mn:O at B, C, and D are 0.7:0.25:1:2.6, 0.65: 0.35:0.89:5.1, and 0.61:0.39:0.70:3.9, respectively. It was assumed that the matrix of the film was stoichiometric.

Both the rods C and D in Fig. 8(d) are originated at the same point at the film–substrate interface, so it is natural that they have the identical derivation trend of element ratio, i.e., Mn deficient and O excess. Mn in C and D was partly substituted with Ti coming from the substrate. At such high deposition temperature ~800 °C, the interfacial diffusion between STO and LCMO is likely to be significant. Since D is closer to the interface than C, more Mn in D was substituted with Ti. Thus, the Ti-$L_{2,3}$ edge in the EELS spectrum acquired from D is relatively intense, as shown in Fig. 9(d). In contrast to rods C and D, only a small amount of Ti appears in rod B and its composition is close to stoichiometric. A slight Ca deficiency in B suggests that the Ca may have been partly substituted for by Sr from the substrate.

The lattice structure of rod B is different from those of C and D. Figures 10(a) and 10(b) show the HREM images of rods B and D displayed in Fig. 8(d), respectively. It can be seen from Fig. 10(a) that rod B preserves the fundamental perovskite structure but is rotated by ~8° with respect to the matrix of the film. A very thin disordered layer at the interface exists between B and the film matrix. The atomic arrangement of rod D is very disordered, as shown in Fig. 10(b), and rod C is even more disordered than D. Clearly, rods C and D do not have a perovskite structure. Note that the oxygen contents of C and D are much higher than that for the ABO_3 structure.

Since almost all of the secondary phase rods are initiated at the film–substrate interface, it is necessary to examine the interfacial structure in detail. Figures 10(c) and 10(d) show HREM images of the interface at E in Fig. 8(d), and an interface where no apparent secondary phase is seen, respectively. Rod E is obviously initiated at the LCMO/STO interface. Although it is highly distorted and not aligned with the matrix of the film, the initial five unit-cell layer seems coherent with the STO substrate. The LCMO film is perfectly coherent with the STO substrate at the interface where there is no apparent secondary phase, as shown in Fig. 10(d). Defects, such as dislocation or stacking faults, are rarely seen. The interface is not sharp, however, possibly due to interfacial reactions during deposition. Not only was no significant tetragonal deformation for the whole film detected by XRD

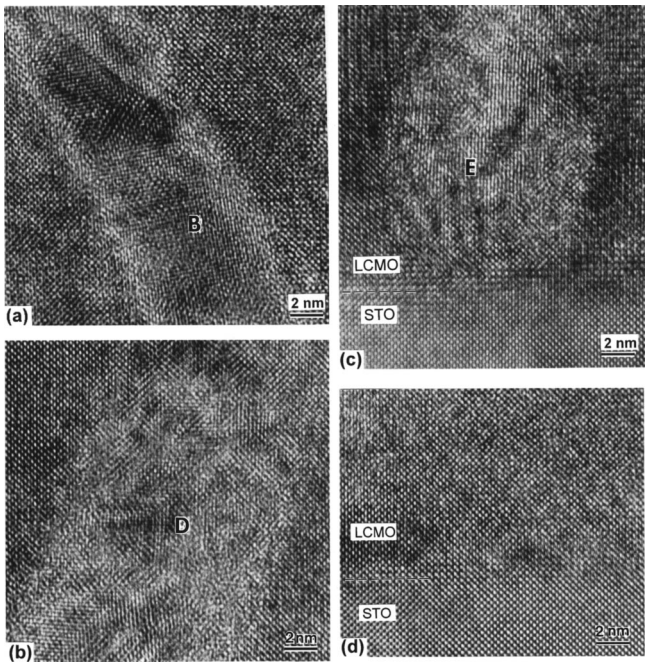

FIG. 10. HREM images at four different positions in Fig. 8(d): (a) B, (b) D, (c) E, and (d) the film–substrate interface where no apparent secondary phase is seen.

(see Table I), but also no significant tetragonal deformation could be found from HREM images close to the LCMO/STO interface.

It seems, therefore, that there are at least two kinds of secondary phases in the LCMO/STO film. One is represented by rods D and C, and the another by rod B. Titanium was diffused into the film mainly along the secondary phase rods such as C and D, while Sr diffused along rods like B in Fig. 8(d). This would be a reasonable suggestion since it is well known that grain boundary diffusion coefficients are ~100–1000 times faster than the self-diffusion coefficients in the bulk.[35] The misfit between the substrate and the film is relaxed into regions of good coherent fit separated by these secondary phases. In fact, the secondary phases act as weak-link grain boundaries.

C. Crystallographic domain structures

The characterization of crystallographic domain structures in the LCMO films is important for studying magnetism, particularly magnetic anisotropy, in these films. In this section, interest is focused on the film orientations with respect to the substrates LAO and STO. The LCMO is a distorted perovskite with a pseudo-cubic lattice parameter of $a_c = 0.3858$ nm. The tilting of the MnO_6 octahedra results in an orthorhombic structure with the space group of $Pnma$ and the lattice parameters of $a \approx b \approx \sqrt{2}a_c$ and $c = 2a_c$.[28]

When LCMO is epitaxially grown on a (001) LAO or STO substrate, six possible domain orientations can coexist in one LCMO thin film, as shown schematically in Fig. 11. For clarity, the pseudocubic perovskite unit cell of LCMO is shown in the figure with orthorhombic indexing of the unit-cell directions. The six possible orientation relationships between the LCMO film and substrates can be described as:

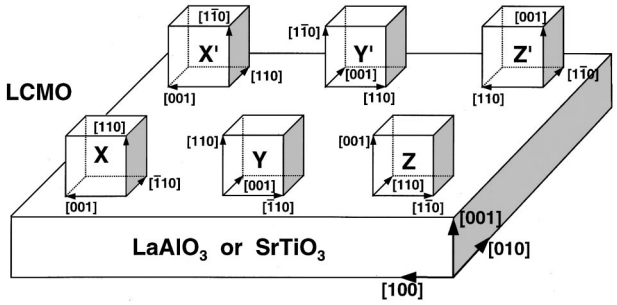

FIG. 11. Schematic diagram showing six possible orientations of epitaxially grown LCMO thin films on the (001) substrates of LAO and STO (consulted that for $SrRuO_3$ in Ref. 36). Note that while the pseudocubic perovskite unit cell of LCMO is drawn, the cell directions are indexed based on the orthorhombic unit cell.

Type X: LCMO(110)[001]//LAO or STO(001)[100],
Type X′: LCMO($1\bar{1}0$)[001]//LAO or STO(001)[100],
Type Y: LCMO(110)[001]//LAO or STO(001)[010],
Type Y′: LCMO($1\bar{1}0$)[001]//LAO or STO(001)[010],
Type Z: LCMO(001)[110]//LAO or STO(001)[010],
Type Z′: LCMO(001)[$1\bar{1}0$]//LAO or STO(001)/[010].

Among the six types of domains in LCMO, X(X′), Y(Y′), and Z(Z′) type domains can be distinguished by means of TEM, while the difference between the X (Y or Z) and X′ (Y′ or Z′) is not distinguishable due to the pseudocubic characteristic of the LCMO structure. In the present work, we only classify the domains in three different types (X, Y, and Z). In fact, the three types of domain orientations correspond to three possible *c*-axis directions of the orthorhombic LCMO, i.e., the *c* axis of LCMO is parallel to the [100], [010], or [001] direction of the substrate, respectively. The domains with the orientation relationships of X or Y type are called [110] oriented and those with Z type are called [001] oriented, since their [110] and [001] axes are perpendicular to the substrate surface, respectively.

Because of the systematic absence of $(00n)$ (n = odd integer) and the degeneracy of d_{110} and d_{002} spacing in the orthorhombic LCMO, it is impossible to distinguish from normal XRD θ-2θ scans whether the film is [110] or [001] oriented or a combination. This ambiguity can be easily resolved by using electron diffraction and HREM. Figure 12 shows the HREM image of a region across a 90° domain boundary in LCMO thin film. The boundary is marked by a dashed line. The arrows denote the *c*-axis directions of individual domains. The typical domain boundaries observed in LCMO films are $90°\{101\}_c$ type. It can be seen that the same type of element meets at the interface. Note that the HREM image along the [001] direction shows a clear doubling periodicity in one (MnO_2) layer out of two, as shown in the lower-right-hand side of the image. A cubic-like structure with *c* axis in the line of sight can be seen from the upper-left-hand side of the image. The insets correspond to the Fourier transformations of the two domains. Except for differences due to a few weak reflections, the two Fourier spectra are identical and they can be indexed with [001] and [110] patterns of the orthorhombic LCMO, respectively.

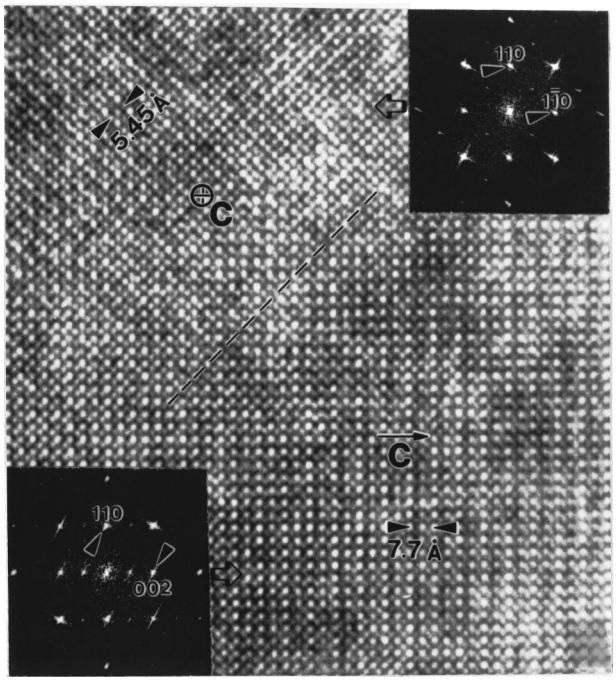

FIG. 12. HREM image of a region across a 90° domain boundary in LCMO thin films. The boundary is marked by a dashed line. Arrowheads denote the *c* directions of individual domains. The insets correspond to the Fourier transformations of the two domains. Note that HREM image along the [001] direction shows a clear doubling periodicity, as shown in the lower-right-hand side of the image. A cubic-like structure with *c* axis in the line of sight can be seen from the upper-left-hand side of the image.

Thus, the orientation of the [001] axis can be easily determined based on Fig. 12.

Based on our SAED and HREM experiments, it was found that both LCMO films grown on LAO and STO consist of domains with different orientation relationship with respect to the substrates. The SAED patterns of Figs. 4(b) and 4(c) consist of at least two patterns of the LCMO superimposed (see insets of Fig. 12), indicating that the film grown on LAO contains variants of the [110] oriented domains with the *c* axis parallel to the substrate surface. A close look at the image of Fig. 4(a) shows that both characteristics of HREM images shown in Fig. 12 can be seen alternately from domain to domain. The *c*-axis directions of different domains are indicated as arrowheads. It is of interest to note that sometimes the secondary phase rods act as domain boundaries, for example, VW and GH in Fig. 4(a). Very small [001] oriented domains were observed occasionally in the LCMO/LAO film. They were usually formed below the bat-shaped rods, as shown in Fig. 6(b). Here the small [001] oriented domain is very close to the substrate–film interface and its size is about 10 nm. It was also observed that such small [001] oriented domains below bat-shaped rods can be far away from the film–substrate interface (~30 nm). This demonstrates that the formation of such small [001] oriented domains is mainly related to the strain field close to the ends of the secondary phase rods. Extensive SAED experiments were carried out in cross-sectional view. It was found that the SAED patterns taken from different areas are similar with the patterns in Fig. 4. Therefore, it can be concluded that the LCMO film grown on LAO is mainly [110] oriented and small [001] oriented domains appear occasionally.

The film grown on STO consists of mixed domains of the [110] and [001] orientations. The SAED pattern of Fig. 8(b) consists of at least three patterns of the LCMO superimposed. It can be seen that the $1/2(001)_c$ spot is much stronger than the $1/2(101)_c$ or $1/2(100)_c$ spot in this pattern, suggesting that the region of the film shown in Fig. 8(a) is dominated by the [001] oriented grains, in agreement with our HREM results. Now the regions shown in Figs. 8(d) and 8(a) are very close together, but the SAED [see the inset of Fig. 8(d)] and HREM experiments demonstrate that the area surrounding the secondary phase rods B, C, D, and E in Fig. 8(d) is dominated by the [110] orientation. The secondary phase rod F in Fig. 8(d) acts as a 90° domain boundary. The left-hand side of F is [110] oriented and the right-hand side [001] oriented. Near the secondary phase rod G in Fig. 8(d) several small [110] oriented domains of the size ~20 nm are formed in the matrix of [001] orientation. Extensive SAED and HREM experiments were carried out in the cross-sectional LCMO/STO sample. It was found that the [001] orientation is dominant in this film.

In order to understand the 90° domain structures present in the LCMO films, the films were also examined in plan view, i.e., with the electron beam normal to the substrate surface. Figures 13(a) and 13(b) show the plan-view TEM images of the LCMO films grown on LAO and STO with their electron diffraction patterns inserted, respectively. The diffraction patterns in Fig. 13 confirm that the films contain multiple orientations, as discussed earlier. The inset in Fig. 13(a) is a superimposition of at least two [110] zone SAED patterns rotated around the zone axis by 90° with respect to one another. The super reflection $1/2(110)_c$ is too weak to be seen. This means that in the LCMO film on LAO the two types of domains, i.e., X and Y type, are rotated around the growth direction with respect to each other by 90°. The domain boundary planes visible in the image of Fig. 13(a) are nearly edge on and are on $\{110\}_c$ planes when indexed according to the pseudocubic unit cell. In the case of the LCMO/STO film, the diffraction pattern taken in plan-view consists of two [110] and one [001] zone SAED patterns superposed, as shown in the inset of Fig. 13(b). Moreover, the super reflection $1/2(110)_c$ in the pattern is much more intense than that in the inset of Fig. 13(a). This confirms that three types of domains are formed in the film on STO and the volume fraction of [001] oriented domains in the film on STO is much higher than that in the film on LAO, as discussed previously. Most of the boundaries visible in the image of Fig. 13(b) are along $\{100\}_c$ directions and they are probably in $\{101\}_c$ planes which are the boundaries between [001] and [110] oriented domains.

IV. DISCUSSION

A. Growth mechanism for secondary phases

The formation of Ca-deficient secondary phase rods in the LCMO/LAO film can be attributed to relieve compressive stress in the plane of the film during the island growth. After a perfectly epitaxial growth of the first 25 nm, LCMO

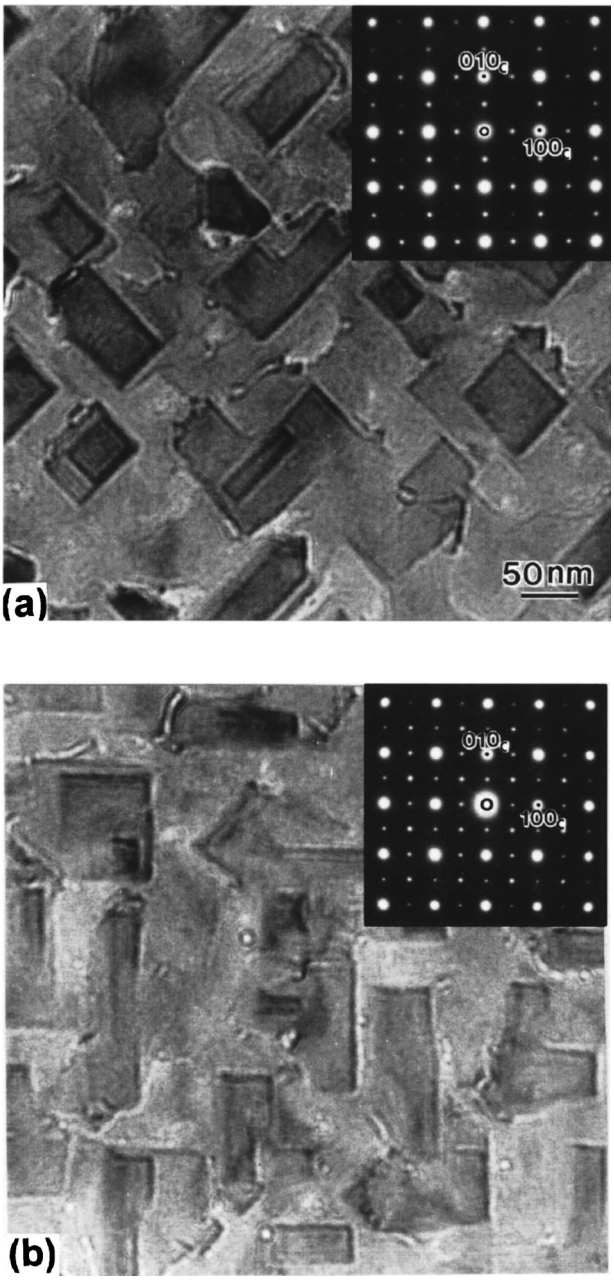

FIG. 13. Plan-view TEM images and electron diffraction patterns of the LCMO thin films grown on (a) (001)LAO, and (b) (001)STO.

islands were nucleated at random and under an in-plane compressive stress. Such a stress can be relieved in part by adopting a structure with a smaller average unit cell. This can be achieved by replacing more La^{+3} ions (>30%) by smaller Ca^{+2} ions (La^{+3} has a radius of 1.02 Å, whereas Ca^{+2} 0.99 Å). Such a substitution simultaneously introduces also Mn^{+4} ions instead of Mn^{+3} and thus decreases somewhat the size of MnO_6 octahedra centered on Mn^{+4} ions. An effective elastic interaction results between Ca^{+2} ions and the stressed layers in the islands. This may lead to a relative increase in the Ca/La ratio of the islands as compared with the space between islands. The composition of such a thick film is thus likely to be inhomogeneous and many Ca-deficient secondary phase rods appear at grain boundaries. In addition, it was found that the oxygen content of the film matrix is lower than that of the secondary phase. This may imply that the initial oxygen deficiency in the islands was caused by the local stress field, which tends to favor structure with a smaller lattice parameter and thus a lower oxygen content.

In the case of the STO substrate, however, LCMO islands were under an in-plane tensile stress, which can be relieved in part by replacing less La^{+3} ions (<30%) by Ca^{+2} ions. This may lead to a decrease in the Ca/La ratio of the islands as compared with the space between islands. Therefore, in such a thick film, many Ca-excess secondary phase rods would appear at grain boundaries. Note that a slight Ca deficiency in rod B in Fig. 8(d) suggests that Ca^{+2} ions in B were partially substituted with Sr^{+2} ions coming from the substrate. It was also found that Ti was mainly diffused into the film along the rods. Possibly due to such diffusion of elements, almost all of the secondary phase rods originated at the LCMO/STO interface. Because Sr^{+2} is larger than Ca^{+2} and Ti^{+3} (or Ti^{+4}) larger than Mn^{+3} (or Mn^{+4}), the interfacial reaction and element diffusion can effectively relieve the in-plane tensile stress. In addition, the higher oxygen content of the rods may also play a role to relax the stress in the film. In this way, the misfit between the substrate and the film is relaxed into regions of good coherent fits separated by these secondary phases.

B. About the formation mechanism of domain structures

The LCMO films have mixed orientations, and different domain structures appear on the LAO and STO substrates. Considering the orthorhombic LCMO as a pseudocubic structure, the crystallographic axes for the cell, a_c, b_c, and c_c are 1/2[110], 1/2[$1\bar{1}0$], and 1/2[001], respectively. Since the pseudocubic parameters are essentially identical in the magnitude, it would be difficult to understand why the [110] orientations should grow preferentially on LAO and [001] preferentially on STO if only the lattice parameter mismatch between the film and substrates is considered.

It may be noted that the angle between 1/2[110] and 1/2[$1\bar{1}0$] of the LCMO is 90.04° while the angle between both the vectors to 1/2[001] is 90°. At room temperature, LAO has a perovskite structure with a slight rhombohedral distortion ($a=0.3788$ nm, $\alpha=90°4'$). LAO experiences a phase transition from a rhombohedral to a cubic structure ($a=0.381$ nm) at 435 °C.[37] $SrTiO_3$ has a cubic perovskite structure with the space group of $Pm\bar{3}m$ and lattice constant of $a=0.3905$ nm.[38] As is well known, the domains in the LCMO films are not necessarily formed during film growth. Distorted (orthorhombic) perovskites usually undergo a phase transition to a more symmetric structure at elevated temperature. For bulk LCMO, differential thermal analysis data indicate a phase transition around 500 °C,[39] which makes it likely that, also in films, the structure at the growth temperature is different from the one at low temperature. In that case, the domains could be formed during cooling of the sample. It was found that strain state and domain structure exhibit a strong correlation.[21] Secondary phases would influence the strain states in the films. Therefore, secondary

phases in the films may play an important role to the formation of domain structures.

Presently, the formation mechanism of the observed 90° domain structures in our LCMO films is not yet clear. It is interesting to compare our results with previous reports. Aarts *et al.*[29] deposited $La_{0.7}Ca_{0.3}MnO_3$ films on STO by sputtering. The LCMO film with a thickness of 5 nm is pure [001] oriented. Mixed domains of [001] and [110] orientations were observed when the films were thicker than 30 nm. Based on their grazing incidence XRD experiments, Rao *et al.*[21] studied the evolution of crystallographic domain orientations of the $La_{0.8}Ca_{0.2}MnO_3$ films grown by PLD on LAO and STO as a function of film thickness. It was found that very thin (<25 nm) films grown on LAO exhibit a pure [110] out-of-plane texture with 90° domains in plane, while those on STO show a single [001] orientation. As film thickness increases, the pure domain orientations are replaced by mixed ones, where both [001] and [110] oriented domains coexist, with the amount of mixture increasing with thickness. For their 100–200 nm thick films on LAO, the volume fraction of [001] oriented domains is in the range of 58%–69%. This result is quite different from our 170 nm thick film grown on LAO, where [001] oriented domains of ~10 nm size can only be seen occasionally. Such a large difference cannot be explained based only on the difference of the chemical composition between their films and our film. It may be related to differences in strain states. Rao *et al.*[21] noted that the rapid in-plane lattice relaxation in $La_{0.8}Ca_{0.2}MnO_3$ films on STO seems to be associated with the initial appearance of the [110] texture. Similarly, the presence of mixed [001] and [110] texture in our film on STO seems related to the almost complete in-plane relaxation, whereas a large residual in-plane compressive stress leads to almost pure [110] texture of our LCMO/LAO film.

C. Microstructure-property relationship

The transport properties of the two films can be explained based on the observed microstructures. We have observed an in-plane compressive stress and a slight tensile stress for the LCMO films grown on LAO and STO, respectively. In addition, our study shows that the interfacial reaction and elemental diffusion have occurred in the film on STO, whereas there is no reaction in the film on LAO where an almost perfect epitaxial growth is accomplished during the initial stage of the film growth. These can explain higher resistivity and lower T_p observed for the LCMO/STO film compared to the film on LAO, since the reaction layer between LCMO and STO as well as secondary phase rods with Ti contamination have higher resistivity than LCMO and increase the effective resistivity of the sample.

Theoretical analysis predicted that the T_c of CMR thin films is extremely sensitive to biaxial strain.[23] This dependence is qualitatively consistent with theoretical models in which the Jahn–Teller electron-phonon coupling plays an important role. Based on lattice parameter arguments alone, T_p for our film on LAO is expected to be lower than that for the film on STO. This is because the biaxial strain of the film on LAO is larger than that for the film on STO and the Jahn–Teller distortion will lead to a localization of electrons and reduce T_c. In contrast, for the film on LAO we see higher T_p. This agrees with Rao *et al.*'s result: while both T_p and strain states exhibit a strong thickness and substrate dependence, no clear correlation between the strain states and T_c could be made.[21] It was suggested that inhomogeneity and disorder in the films were responsible for the lack of correlation. Our microstructure study shows that nonstoichiometric secondary phases and orientation disorder indeed play a role in influencing the electrical properties of LCMO films.

The difference in the crystalline texture of the films may also affect the resistivity and T_p, since the film on LAO exhibits an almost pure [110] texture with 90° domains while the film on STO has mixed [001] and [110] textures. However, it is not clear whether the LCMO films containing 90° domains and mixed textures of [001] and [110] have different resistivity since LCMO has almost isotropic characteristics. Also the LCMO films by Rao *et al.*[21] have different textures compared with our samples, their films on LAO have mixed [001]/[110] textures. Hence, the differences in the crystalline texture may not be the major factor determining the differences in resistivity and T_p.

Wang *et al.*[18] reported low-field magnetoresistance in $Pr_{0.67}Sr_{0.33}MnO_3$ ultrathin films and interpreted the results based on the strain-induced magnetic anisotropy and domain motion. The $Pr_{0.67}Sr_{0.33}MnO_3$ films show unusually large low field MR. In most cases, however, the domain motion produces very small magnetoresistance.[40] However, we believe that the secondary phase rods and defects observed in our films can provide an explanation for the large MR related to the domain motion/magnetization. Peng *et al.*[41] observed necklace-like grain chains in $La_{0.5}Ca_{0.5}MnO_3$ films with large low-field MR. They suggested that the microchains serve as weak-link grain boundaries and may enhance the low-field MR response. The chains are likely to be secondary phases similar to the rods observed in our films.

V. CONCLUSIONS

LCMO thin films with a thickness of ~170 nm were grown on (001) LAO and (001) STO substrates. The substrate-film lattice mismatch causes changes in the microstructure of the films and can therefore influence their resistive and magnetoresistive properties. The LCMO/LAO film shows a higher T_p and lower resistivity than the film on STO.

The microstructures (including strain state, surface morphology, secondary phases, crystallographic domain structure, interface, and defect) of both films were characterized by XRD, AFM, TEM, HREM, and EELS. The film on LAO is under a large compressive strain while the film on STO under a smaller tensile strain. Both films exhibited an island growth surface morphology. Numerous secondary phase rods were formed in both films and these act as weak-link grain boundaries (and sometimes also as domain boundaries). For the film on LAO, almost all the secondary phase rods were Ca deficient and originated in the film after a thickness of about 25 nm and then grew to the film surface. A perfectly

epitaxial LCMO layer of the thickness ~25 nm was formed near the film–substrate interface. No apparent interfacial reaction occurred between the LCMO and the LAO and discrete dislocations were observed at the interface. The LCMO film grew on LAO layer by layer in the initial stage up to about 25 nm and then changed to island growth. The formation of Ca-deficient secondary phases can be attributed to relieve compressive stresses in the plane of the film during the island growth. In the case of the STO substrate, however, almost all of the secondary phase rods initiated at the film–substrate interface. Some of them penetrated the entire thickness of the film, while others ended in the bulk of the film. The misfit between STO and LCMO was relaxed into regions of good coherent fit separated by such secondary phases. It was apparent that some interfacial reaction had occurred and titanium was found to have diffused into the film, mainly along the secondary phase rods.

The two types of substrates lead to the formation of two corresponding domain structures in the LCMO films. The film on LAO exhibits a nearly pure [110] out-of-plane texture with 90° domains in plane, and only very small [001] oriented domains can be found. In contrast, the film grown on STO consists of mixed domains of [001] and [110] orientations with the [001] orientation dominant. These domain structures seem linked with strain states and the secondary phases grown in the films may play an important role to the formation of domain structures.

These microstructural aspects must be considered when interpreting the properties of such films and comparing the results of different experiments. Certain key questions, such as the details of the formation mechanisms of the observed domain structures, strain states at the growth temperature and T_c, the chemical composition and crystal structure of the secondary phases, still remain to be addressed.

ACKNOWLEDGMENTS

The research carried out at Beijing Laboratory of Electron Microscopy, Institute of Physics, Chinese Academy of Sciences was supported by the National Natural Science Foundation of China (5982550). C. J. Lu was also supported by the National Natural Science Foundation of China (19804004) and by China Postdoctoral Science Foundation. We would like to thank Professor K. H. Kuo for his interest and support for this study. Professor X. F. Duan, Professor R. H. Wang, and Professor M. X. Dai are also thanked for helpful discussions. The work at Los Alamos was a Los Alamos National Laboratory Directed Research and Development Project supported by the United States Department of Energy.

[1] R. von Helmholt, J. Wecker, B. Holzapfel, L. Schultz, and K. Sammer, Phys. Rev. Lett. **71**, 2331 (1993).
[2] K. Chahara, T. Ohno, M. Kasai, and Y. Kozono, Appl. Phys. Lett. **63**, 1990 (1993).
[3] S. Jin, T. H. Tiefel, M. McCormack, R. A. Fastnaacht, R. Ramesh, and L. H. Chen, Science **264**, 413 (1994).
[4] A. Urushibara, Y. Moritomo, T. Arima, A. Asamitsu, G. Kido, and Y. Tokura, Phys. Rev. B **51**, 14103 (1995).
[5] C. N. R. Rao, A. K. Cheetham, and R. Mahesh, Chem. Mater. **8**, 2421 (1996); C. N. R. Rao and A. K. Cheetham, Science **272**, 369 (1996).
[6] P. B. Tavares, V. S. Amaral, J. P. Araujo, J. B. Sousa, A. A. C. S. Lourenco, and J. M. Vieira, J. Appl. Phys. **85**, 5411 (1999).
[7] K. A. Thomas, P. S. I. P. N. de Silva, L. F. Cohen, A. Hossain, M. Rajeswari, T. Venkatesan, R. Hishes, and J. L. MacManus-Driscoll, J. Appl. Phys. **84**, 3939 (1998).
[8] E. S. Vlakhov, R. A. Chakalov, R. I. Chakalova, K. A. Nenkov, K. Dorr, A. Handstein, and K. H. Muller, J. Appl. Phys. **83**, 2152 (1998).
[9] Y. Suzuki, H. Y. Hwang, S.-W. Cheong, and R. B. van Dover, Appl. Phys. Lett. **71**, 140 (1997).
[10] C. Zener, Phys. Rev. **82**, 403 (1951).
[11] G.-M. Zhao, K. Conder, H. Keller, and K. A. Müller, Nature (London) **381**, 676 (1996).
[12] A. J. Millis, P. B. Littlewood, and B. I. Shraiman, Phys. Rev. Lett. **74**, 5144 (1995).
[13] E. Müller-Hartmann and E. Dagotto, Phys. Rev. B **54**, R6819 (1996).
[14] H. Y. Hwang, S.-W. Cheong, P. G. Radaeli, M. Marezio, and B. Batlogg, Phys. Rev. Lett. **75**, 914 (1995).
[15] J. Fontcuberta, B. Martinez, A. Seffer, S. Pinol, J. L. Garcia-Munoz, and X. Obradors, Phys. Rev. Lett. **76**, 1122 (1996).
[16] Y. Moritomo, A. Asamitsu, and Y. Tokura, Phys. Rev. B **51**, 16491 (1995).
[17] K. Khazeni, Y. X. Jia, Li Lu, V. H. Crespi, M. L. Cohen, and A. Zettl, Phys. Rev. Lett. **76**, 295 (1996).
[18] H. S. Wang, Q. Li, K. Liu, and C. L. Chen, Appl. Phys. Lett. **74**, 2212 (1999).
[19] C. Kwon, M. C. Robson, K.-C. Kim, J. Y. Gu, S. E. Lofland, S. M. Bhagat, Z. Trajanovic, M. Rajeswari, T. Venkatesan, A. R. Kratz, R. D. Gomez, and R. Ramesh, J. Magn. Magn. Mater. **172**, 229 (1997).
[20] E. Gommert, H. Cerva, J. Wecker, and K. Samwer, J. Appl. Phys. **85**, 5417 (1999).
[21] R. A. Rao, D. Lavric, T. K. Nath, C. B. Eom, L. Wu, and F. Tsui, Appl. Phys. Lett. **73**, 3294 (1998).
[22] T. K. Nath, R. A. Rao, D. Lavric, C. B. Eom, L. Wu, and F. Tsui, Appl. Phys. Lett. **74**, 1615 (1999).
[23] A. J. Millis, T. Darling, and A. Migliori, J. Appl. Phys. **83**, 1588 (1998).
[24] P. Lu, F. Chu, Q. X. Jia, and T. E. Mitchell, J. Mater. Res. **13**, 2302 (1998).
[25] Z. L. Wang and J. Zhang, Phys. Rev. B **54**, 1153 (1996).
[26] Z. L. Wang and J. S. Yin, Philos. Mag. B **77**, 49 (1998).
[27] Z. L. Wang and Z. C. Kang, in *Functional and Smart Materials—Structural Evolution and Structure Analysis* (Plenum, New York, 1998).
[28] O. I. Lebedev, G. Van Tendeloo, S. Amelinckx, B. Leibold, and H.-U. Habermeier, Phys. Rev. B **58**, 8065 (1998); J. Aarts, S. Freisem, R. Hendrikx, and H. W. Zandbergen, Appl. Phys. Lett. **72**, 2975 (1998).
[29] E. Gommert, H. Cerva, A. Rucki, R. von Helmolt, J. Wecker, C. Kuhrt, and K. Samwer, J. Appl. Phys. **81**, 5496 (1997).
[30] J. Aarts, S. Freisem, R. Hendrikx, and H. W. Zandbergen, Appl. Phys. Lett. **72**, 2975 (1998).
[31] N.-C. Yeh, R. P. Vasquez, D. A. Beam, C.-C. Fu, J. Huynh, and G. Beach, J. Phys.: Condens. Matter **9**, 3713 (1997).
[32] M. E. Hawley, C. D. Adams, P. N. Arendt, E. L. Brosha, F. H. Garzon, R. J. Houlton, M. F. Hundley, R. H. Heffner, Q. X. Jia, J. Neumeier, and X. D. Wu, J. Cryst. Growth **174**, 455 (1997).
[33] Y. H. Li, K. A. Thomas, P. S. I. P. N. de Silva, L. F. Chen, A. Goyal, M. Rajeswari, N. D. Mathur, M. G. Blamire, J. E. Evetts, T. Venkatesan, and J. L. MacManus-Driscoll, J. Mater. Res. **13**, 2164 (1998).
[34] C. Ritter, M. R. Ibarra, J. M. De Teresa, P. A. Algarabel, C. Marquia, J. Blasca, J. Garcia, S. Oseroff, and S.-W. Cheong, Phys. Rev. B **56**, 8902 (1997).
[35] A. D. LeClaire, Br. J. Appl. Phys. **14**, 351 (1963).
[36] J. C. Jiang, W. Tian, X. Q. Pan, Q. Gan, and C. B. Eom, Appl. Phys. Lett. **72**, 2963 (1998).
[37] S. Geller and V. B. Bala, Acta Crystallogr. **9**, 1019 (1956).
[38] W. Bensch, H. W. Schmalle, and A. Reller, Solid State Ionics **43**, 171 (1990).
[39] T.-W. Li (private communication).
[40] Y. Wu, Y. Suzuki, U. Rüdiger, J. Yu, A. D. Kent, T. K. Nath, and C. B. Eom, Appl. Phys. Lett. **75**, 2295 (1999).
[41] H. B. Peng, B. R. Zhao, Z. Xie, Y. Lin, B. Y. Zhu, Z. Hao, Y. M. Ni, H. J. Tao, X. L. Dong, and B. Xu, Appl. Phys. Lett. **74**, 1606 (1999).